Infrared Physics & Technology 145 (2025) 105668

Contents lists available at ScienceDirect

Infrared Physics and Technology

journal homepage: www.elsevier.com/locate/infrared

Research Paper

Sub-wavelength optical modulation of step-size varying infrared photodetectors

Min Luo [a,d,1], Haonan Ge [a,1], Shuning Liu [a,b], Runzhang Xie [a,*], Fang Zhong [a,c,*]

[a] State Key Laboratory of Infrared Physics, Shanghai Institute of Technical Physics, Chinese Academy of Sciences, Shanghai 200083, China
[b] Thrust of Microelectronics, Function Hub, The Hong Kong University of Science and Technology (Guangzhou), Guangzhou 511453, China
[c] Hangzhou Institute for Advanced Study, University of Chinese Academy of Sciences, Hangzhou 310024, China
[d] University of Chinese Academy of Sciences, Beijing 100049, China

ARTICLE INFO

Keywords:
Black phosphorus
Optical field enhancement
Infrared detection
Sub-wavelength focusing

ABSTRACT

Low-dimensional materials, particularly black phosphorus, show exceptional promise for applications in photoelectric sensors due to their high carrier mobility, tunable band gap, and remarkable electrical properties. Black phosphorus, typically obtained through mechanical exfoliation, often exhibits uneven layer thickness, leading to the spontaneous formation of natural heterojunctions. These heterojunctions, characterized by extremely narrow channels, are conducive to enhanced built-in electric fields and improved conductivity, which collectively enhance the detectivity of the devices. To further optimize the interaction between light and matter, we propose a design featuring geometric patterns with varying parameters surrounding the device. Geometric patterns are strategically engineered to enhance the electromagnetic field, thereby fostering a more robust light-matter interaction. As a result, the photon-generated carriers benefit from an efficient separation rate while maintaining a high diffusion velocity. This design approach not only enhances the performance of black phosphorus-based photoelectric sensors but also opens new avenues for the development of advanced optoelectronic devices. Our findings suggest significant implications for the practical use of black phosphorus in next-generation photoelectric applications, including imaging, sensing, and light-harvesting technologies.

1. Introduction

Two-dimensional materials, particularly those belonging to the van der Waals family, have garnered immense interest in recent years due to their unique and diverse properties, which present promising applications in infrared detection [1–3]. The unique ability of these materials to be stacked into vertical heterojunctions without the constraints of lattice mismatches due to their non-polar surfaces and lack of surface hanging bonds addresses many of the interface state challenges commonly encountered in traditional semiconductor materials [4,5]. This characteristic not only facilitates the construction of high-performance optoelectronic devices but also paves the way for innovative device architectures that can leverage the advantages of two-dimensional materials [6–9].

Despite the remarkable performance of two-dimensional materials, their inherently thin structure poses significant limitations in terms of light absorption capacity. To tackle this challenge and maximize light-matter interactions, researchers have proposed the integration of optical resonators and waveguide structures, enhancing the interaction between incident light and the two-dimensional materials [10–12]. A key advantage of photodetectors equipped with optical waveguide structures is their ability to fully utilize evanescent waves, thereby optimizing light interaction with the two-dimensional materials. This capability is particularly beneficial for applications within integrated optics, where miniaturization and efficiency are paramount [13–16].

Though the advancements in two-dimensional materials for infrared detection are noteworthy, several challenges must be addressed before widespread practical applications can be realized. A prominent issue is determining how to effectively exploit the ultra-thin nature of these materials without compromising their sensitivity to infrared signals [17–19]. Among these materials, black phosphorus stands out as a promising candidate, characterized by its high carrier mobility and

* Corresponding authors at: State Key Laboratory of Infrared Physics, Shanghai Institute of Technical Physics, Chinese Academy of Sciences, Shanghai 200083, China (F. Zhong).
E-mail addresses: xierunzhang@mail.sitp.ac.cn (R. Xie), zhongfang@ucas.ac.cn (F. Zhong).
[1] These two authors contributed equally to the work.

https://doi.org/10.1016/j.infrared.2024.105668
Received 10 October 2024; Received in revised form 6 December 2024; Accepted 9 December 2024
Available online 11 December 2024
1350-4495/© 2024 Elsevier B.V. All rights are reserved, including those for text and data mining, AI training, and similar technologies.

tunable bandgap, which ranges between 0.3 eV and 2 eV. This tunable range includes conventional semiconductor bandgap values, such as approximately 1.12 eV for silicon and 1.44 eV for GaAs [20]. Its ability to exhibit a bandgap that spans from the visible to the mid-infrared region, coupled with anisotropic electronic and optical properties, positions black phosphorus as a suitable material for developing high-performance electronic and optoelectronic devices, quantum applications, and potentially superconducting systems, thereby enhancing its prospects for high-sensitivity mid-infrared optoelectronic devices [21–26].

Nonetheless, the controlled growth of multi-layer black phosphorus (BP) films remains a significant hurdle since its discovery, hampering further research and practical applications. Current methods for scaling exfoliated black phosphorus thin films often yield inconsistent and irregular shapes. Furthermore, as the number of layers increases, the overlap of wave functions at the valence band maximum and conduction band minimum leads to hybridization, forming bonding and anti-bonding states that cause notable changes in energy distribution and material properties [27–29].

Mechanical exfoliation is the most common approach for obtaining two-dimensional materials in laboratory settings; however, it typically suffers from limitations regarding precise control over thickness, size, and shape, often resulting in uneven and intrinsic junctions [30]. In light of these challenges, we propose a solution that involves creating regular, elongated, and narrow trenches through etching layers of black phosphorus. Additional artificial geometric structure aims to enhance carrier separation efficiency and improve both the detection rate and sensitivity of the photodetector through photoelectric co-regulation [31,32]. By integrating such innovative strategies, we may address existing limitations and unlock the full potential of two-dimensional materials for future optoelectronic applications.

2. Method

To maximize the separation efficiency of photogenerated carriers, it is important to create as large a carriers density gradient as possible. In this work, we try to maximize the concentration of photogenerated carriers in the built-in electric field region by introducing photonic structures to focus the optical field, thereby concentrating the position the photogenerated carriers generated. Additionally, by introducing quasi-one-dimensional charge transport channels, we minimize the concentration gradient in directions perpendicular to the built-in electric field, concentrating the diffusion current while maximizing the use of the built-in electric field caused by layer number variations to distinguish photogenerated electrons and holes.

Narrower channels can reduce the shielding effect of equilibrium carriers on the built-in electric field, thus effectively broadening the distribution of the built-in electric field and enhancing its role in distinguishing photogenerated electrons and holes. In quasi-one-dimensional structures, the dielectric function of the ideal built-in electric field must be replaced by an effective dielectric function, which is a composite system of semiconductor materials, substrate, and air. This effective dielectric function is a weighted average of the dielectric functions of the semiconductor, substrate, and air, with the accurate values varying with specific position and depending on the three-dimensional structure of the device. According to effective medium theory, the lower bound of this dielectric function is the harmonic mean when the weights of the substrate and air are both 50 %. Given the theoretical limit of the broadened built-in electric field distribution, device design must take into account carrier accumulation at the edges of the built-in electric field, where the drift current decreases due to the weakening of the field. Longer device channels have higher resistance, and using the built-in electric field enables low dark current performance operating under zero bias. By integrating sub-wavelength photonics with nanoelectronics to modulate the optoelectronic and transport processes, the carrier separation efficiency in the device can be significantly improved.

In this study, we analyze key parameters affecting the performance of a semiconductor device, as illustrated in Fig. 1b. The parameters include the channel lengths of thin-layer (L_1) and thick-layer (L_2) black phosphorus, with a channel width denoted as W_1. Additionally, we define the dimensions of the sphenoid thin black phosphorus as L_3 and W_2, and the distance from the electrode to this material as L_4. Our analysis will explore how these parameters influence the built-in electric field and photogenerated carrier separation efficiency through theoretical computations and simulations.

The device schematic graph specifies a thin-layer material thickness of 5 nm (approximately 7 layers) with a doping concentration of 1×10^{15} cm^{-3}, and a thick layer material thickness of 10 nm (around 14 layers) with a concentration of 6×10^{15} cm^{-3} [33,34]. The channel lengths are set at $L_1 = 1$ μm and $L_2 = 0.3$ μm, with channel width $W_1 = 0.02$ μm. The sphenoid thin layer has dimensions $L_3 = 1$ μm and $W_2 = 2$ μm, while the distance from the electrode to the material edge is $L_4 = 1$ μm. A voltage of $V_{ds} = \pm 0.5$ V is applied to the device's source and drain.

Utilizing the finite element method, we constructed the schematic representation of the semiconductor device illustrated in Fig. 1. The yellow areas at the left and right ends of the device structure are the electrodes set during simulation, the left electrode is marked V_1, and the right electrode is marked V_2. The thin layer region has been assigned a thickness of 5 nm, whereas the thick layer has a thickness of 10 nm. The energy band curve distribution and the internal electric field of the device are obtained by solving the governing equations of semiconductors for various conditions, including different bias voltages, quasi-Fermi level positions, slit widths, and lengths when $G_{opt} = 0$ [35,36].

$$\nabla\cdot(-\varepsilon_0\varepsilon_e\nabla V) = \rho \tag{1}$$

$$\nabla\cdot\boldsymbol{J}_n = q(R - G_{opt}) + q\frac{\partial n}{\partial t} \tag{2}$$

$$-\nabla\cdot\boldsymbol{J}_p = q(R - G_{opt}) + q\frac{\partial n}{\partial t} \tag{3}$$

$$\nabla\cdot(-\varepsilon_0\varepsilon_e\nabla V) = q\left(p - n + N_d^+ - N_a^-\right) \tag{4}$$

$$G_{opt} = \frac{1}{\hbar}\varepsilon_0 n\kappa E_0^2 \tag{5}$$

Then, the optical field distribution data excited by micro and nano structures is taken as the production term and put into the current continuity equation in the semiconductor equation to calculate the separation efficiency of photogenerated carriers, and the separation efficiency of photogenerated carriers under different optical field distributions is obtained [37–39].

$$\nabla\times(\nabla\times\boldsymbol{E}) + \frac{\varepsilon}{c^2}\frac{\partial^2\boldsymbol{E}}{\partial t^2} = 0 \tag{6}$$

$$G_{opt} = \frac{1}{\hbar}\varepsilon_0\varepsilon''|E|^2 \tag{7}$$

By solving the electromagnetic wave equation using the finite-difference time-domain (FDTD) method, we obtain the three-dimensional (3D) distribution data of the local electric field E resulting from the coupling of micro and nano structures with the incident optical field. This 3D electric field distribution is then interpolated to construct an abstract function that describes the relationship between the optical field E and the spatial coordinates x ,y, and z. Subsequently, this abstract function E is integrated into the generation term G_{opt} of the semiconductor equations. The finite element method is employed to solve these semiconductor equations, allowing us to analyze the separation efficiency and conductivity of the photogenerated carriers under various conditions. The dielectric constant information of the material comes from related article [40].

In the model structure of light field simulation calculation by finite-

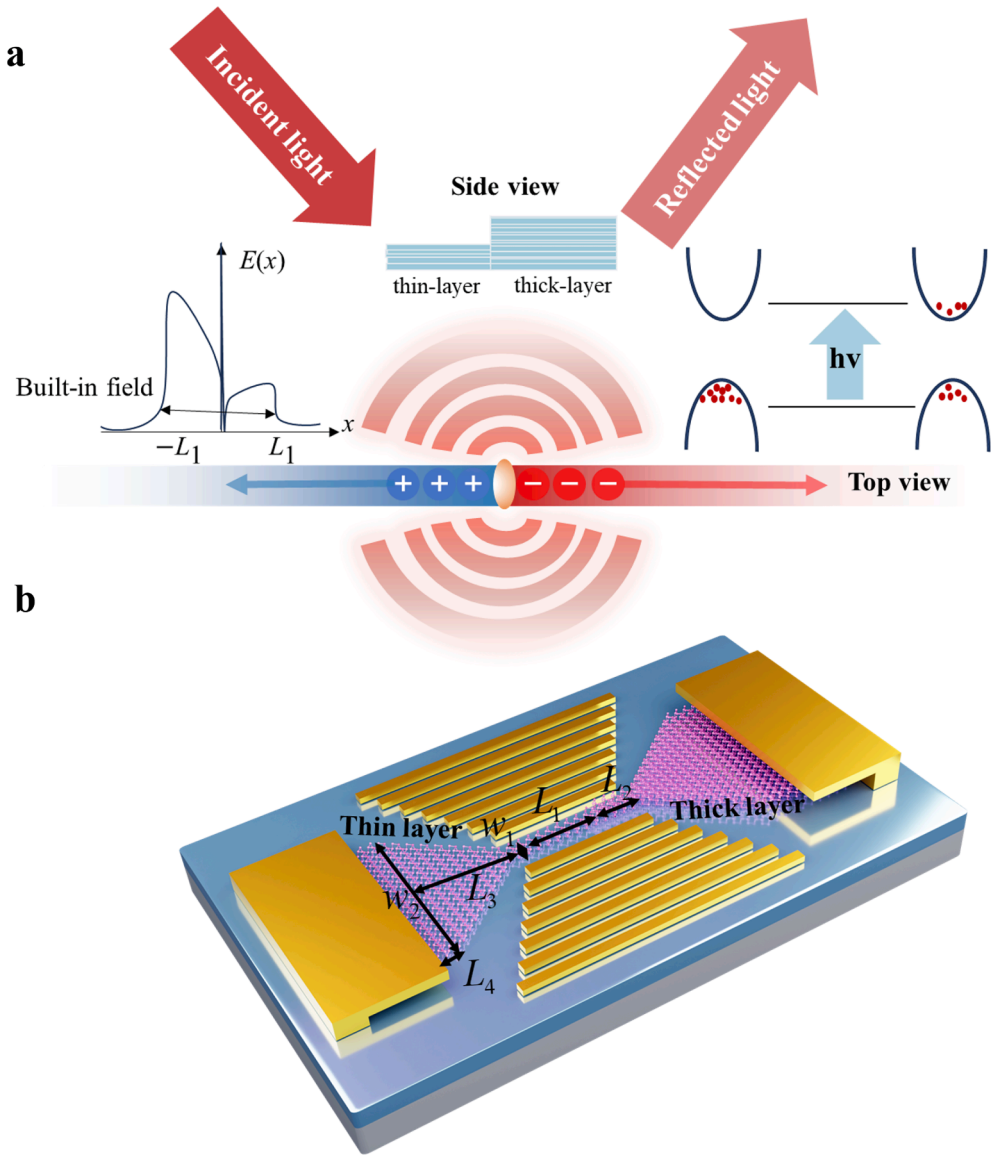


Fig. 1. (a) Schematic diagram of device working principle: photogenerated carrier generation, separation, and subwavelength localization in narrow channel heterojunctions induced by variations in natural layer thickness (b) Geometric representation of the device as modeled in COMSOL.

difference time-domain algorithm, the upper and lower boundary adopts perfectly matched layer (PML) boundary, the left and right boundary adopts PML boundary, the light source is selected as the plane wave incident, and the light source is 1.5 μm away from the micro and nano structure in the axis position. The wavelength range is 1.3–1.7 μm, and the meshes of micro-nano structure region are $d_x = d_y = 0.02$ μm, $d_z = 0.005$ μm. The abstract function of the optical field I and the space coordinates x ,y, z is obtained by interpolating the optical field obtained from the simulation, and coupled to the semiconductor equation as the production term G in the semiconductor simulation model.

3. Results and Discussion

Fig. 2a displays the electric field distribution obtained through numerical simulations from top view of the device. X-axis represents the length direction and Y-axis represents the width direction. X = 0 is the interface between the thick layer and the thin layer. Our findings reveal that thicker layers of black phosphorus generate a stronger electric field, while thinner layers yield a smoother distribution. In thin-layer heterojunctions, the electric field is concentrated at the interface, enhancing charge carrier migration and consequently affecting the device's conductivity. In contrast, thicker heterojunctions exhibit a more uniform electric field distribution, leading to slower carrier migration, which could impact switching characteristics. The difference between thin-layer and thick-layer materials is influenced by a variety of factors, including network effects and microscopic mechanisms, for example an increase in the band gap by quantum confinement effects, local electric field effect, more significant surface and interface effects of thin layer materials.

Fig. 2b presents the simulated current–voltage (*IV*) characteristics of the device in the dark state from 77 K to 300 K. The observed asymmetry in current between positive and negative voltage regions indicates distinct rectifying behavior. The minimal reverse dark current saturates with increasing reverse bias, illustrating the good insulating properties of the heterojunction.

To further elucidate the dark current behavior, we simulated the band structure under various bias voltages. Fig. 2c shows that with no bias, the valence and conduction bands of the thick layer material are positioned above and below those of the thin layer, respectively. This arrangement causes charge carriers to accumulate without separation.

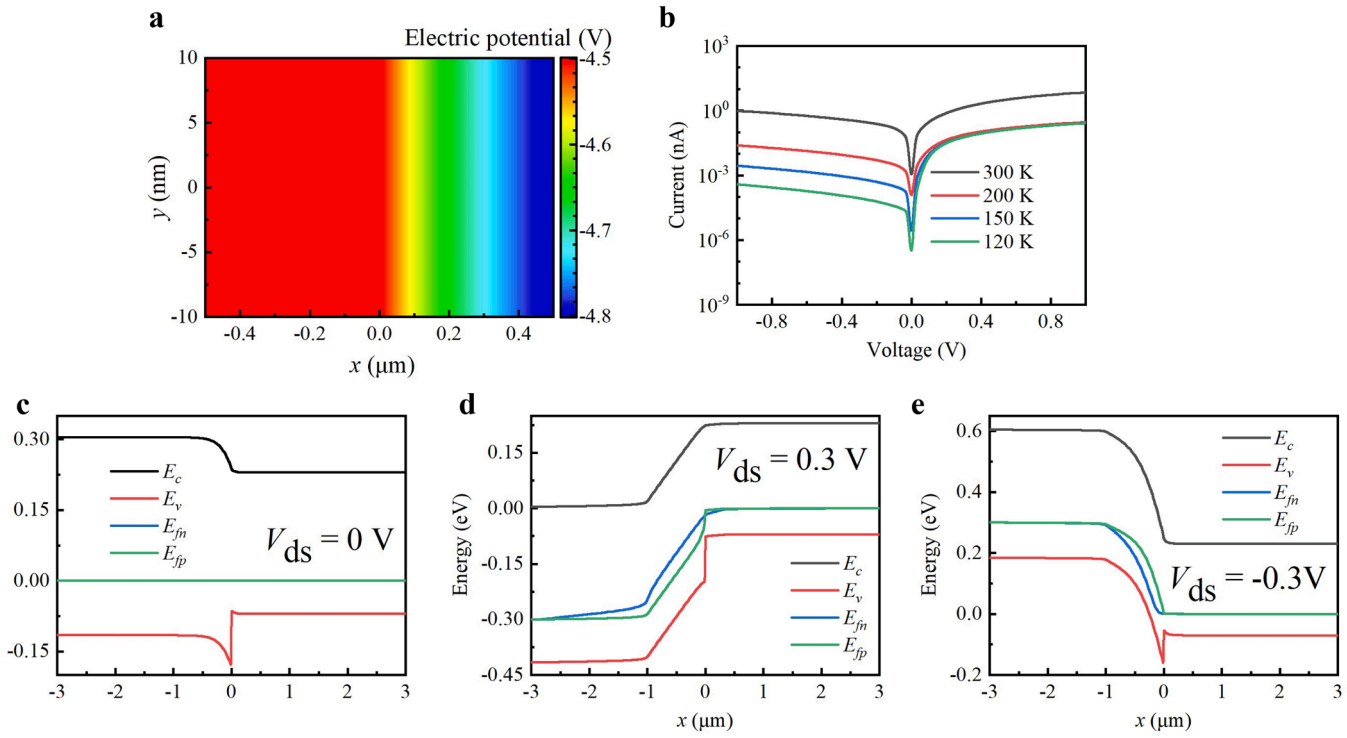


Fig. 2. Potential distribution and band structure of device conducted through simulation (a) Two-dimensional potential distribution diagram of the device (Top view of device). (b) Characterization of the dark current of the device in different temperature. (c) Simulated band structure of the device at V_{ds} = 0 V. (d) Simulated band structure of the device at V_{ds} = 0.3 V. (e) Simulated band structure of the device at V_{ds} = -0.3 V.

In Fig. 2d, under reverse bias, the conduction and valence bands of the thick layer material drop below those of the thin layer, preventing electron and whole movement to the thin layer, resulting in a small current. Conversely, Fig. 2e illustrates that during forward bias, the thick layer's bands rise above those of the thin layer, enabling the electric field created by the band structure to assist in charge carrier separation, thus generating a larger dark current.

To investigate the impact of various parameters on the built-in electric field within the device, we conducted simulations with differing channel lengths, widths, and applied source voltages, the results are presented in Fig. 3.

In Fig. 3a, we observe that with a channel length of ($L_1 = 0.5$ μm) and under reverse bias, the built-in electric field width measures approximately (0.5 μm), coinciding with the channel length. The electric field is concentrated at the interface between the thin-layer and thick-layer materials, exhibiting a decay in potential as one approaches the thin layer. Stronger reverse bias leads to an enhanced built-in electric field with a slower decay rate. Conversely, Fig. 3b depicts the behavior of the built-in electric field under forward bias. Here, the electric field shows an asymmetric distribution at the contact boundary, with a greater intensity in the thin-layer region compared to the thick-layer region. A noticeable discontinuity occurs at the boundary; as the forward bias increases, the built-in electric field intensifies.

In Fig. 3c and d, while maintaining a reverse bias of ($V_{ds} = -0.3$ V), we varied the channel length. The results indicate that as the channel length increases, the width of the built-in electric field also widens, approximately equal to the channel length. Under fixed positive bias (V_{ds} = 0.3 V), the maximal built-in electric field is observed at the interface. However, the electric field size and width in the thin layer remain constant regardless of channel length, while the width in the thick layer aligns with the channel length, revealing no significant variation in electric field strength.

Fig. 3e and f show that fixing the channel length at (L_1 = 0.5 μm) while applying a reverse bias of (V_{ds} = -0.3 V) has no effect on the built-in electric field's strength and width relative to channel width, which remains approximately equal to the channel length. Under fixed forward bias (V_{ds} = 0.3 V), while the intensity and magnitude of the built-in electric field in the thick layer region remain unaffected by channel width, the thin layer region displays a variance whereby narrower channels yield an increased electric field intensity.

In summary, the distribution of the built-in electric field is influenced by the applied voltages, exhibiting distinctive behaviors under positive and negative biases. Under positive bias, the electric field demonstrates an asymmetric distribution, favoring the thin layer, while under reverse bias, the field decays from the material boundary into the thin layer. The width of the built-in electric field corresponds to the channel length, whereas its strength is contingent upon the channel width and the magnitude of the applied bias voltage.

The channel length significantly influences the path length of carrier movement within the material, thereby affecting the behavior of the built-in electric field, which governs carrier dynamics. A longer channel length necessitates that carriers experience the effects of the built-in electric field over a greater distance, leading to an expanded influence range of this electric field.

When a forward bias is applied, electrons and holes migrate in opposite directions due to the electric field. Given that the physical properties (e.g. band structure, carrier concentration) of the thin-layer and thick-layer materials can differ, this variance results in an asymmetric distribution of the built-in electric field at their interface. Thin-layer materials typically exhibit a higher surface-area-to-volume ratio, which facilitates the accumulation of charge, thereby intensifying the built-in electric field in the thin-layer region.

In contrast, applying a reverse voltage inhibits the normal flow of carriers, causing them to accumulate at the material boundary. As the distance from this boundary increases toward the thin-layer material, the carrier concentration gradually decreases, resulting in a decay of the internal electric field from the material boundary into the thin layer.

A narrower channel width enhances interactions among carriers, as the Coulombic forces become more pronounced in confined regions, often leading to an increase in built-in electric field strength. Conversely,

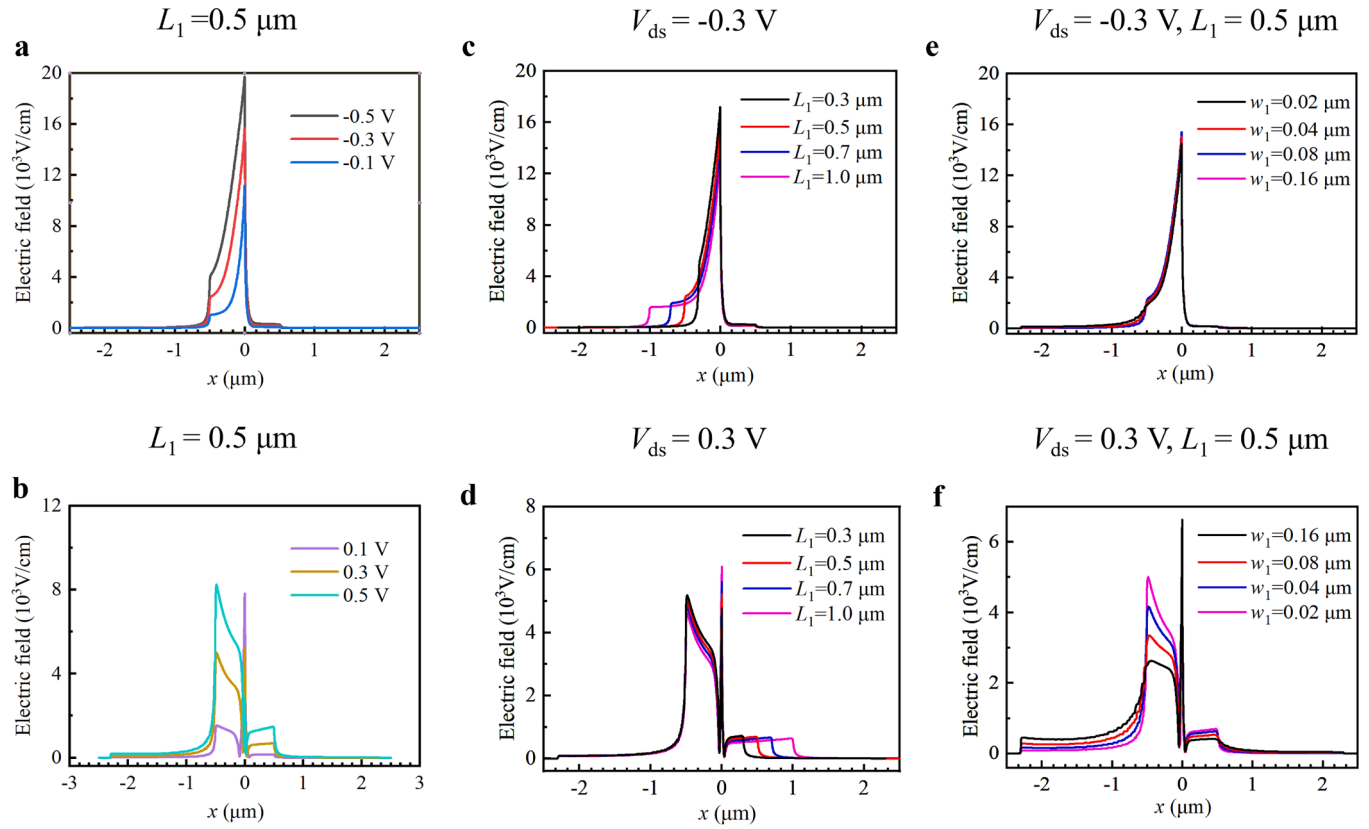


Fig. 3. Effect of different parameters on built-in electric filed. (a) The simulated results of the built-in electric field with a length (L_1) of 0.5 μm under negative bias conditions are presented for V_{ds} values of −0.1 V, −0.3 V, and −0.5 V. (b) The simulated outcomes of the built-in electric field with L_1 set to 0.5 μm are examined under positive bias conditions, specifically for V_{ds} values of 0.1 V, 0.3 V, and 0.5 V. (c) The impact of varying L_1 values (0.3 μm, 0.5 μm, 0.7 μm, and 1.0 μm) on the built-in electric field is simulated under a bias of V_{ds} = -0.3 V. (d) The effects of different L_1 lengths (0.3 μm, 0.5 μm, 0.7 μm, and 1.0 μm) on the built-in electric field are evaluated under a positive bias of V_{ds} = 0.3 V. (e) The simulations of the built-in electric field are also conducted by varying the width (w1) under a negative bias of V_{ds} = -0.3 V, while maintaining L_1 at 0.5 μm. (f) the simulated results for the built-in electric field, with differing w_1 values under a positive bias of V_{ds} = 0.3 V and L_1 fixed at 0.5 μm.

in wider channels, the dispersion of carriers weakens these interactions, resulting in a relatively lower intensity of the internal electric field. Additionally, a higher applied bias amplifies the driving forces on the internal charges, promoting greater charge separation and thus a stronger built-in electric field. Conversely, with a smaller applied bias, charge separation diminishes, leading to a weaker built-in electric field.

Shorter channel lengths correlate with more effective internal electric field actions, which can enhance carrier collection efficiency and response speed, consequently increasing detector sensitivity. Moreover, shorter channels typically reduce noise generation; the concentrated influence of the internal electric field over shorter distances helps mitigate noise and improve the signal-to-noise ratio of the detector. With shorter channel lengths, carriers traverse smaller distances, leading to reduced scattering and energy losses, thereby maximizing transmission efficiency. As a result, the built-in electric field can interact with carriers more effectively in shorter channels, further enhancing transmission efficiency.

As Fig. 4a, b and c show, the artificial geometric structure is a prominent nano-optical design known for its high sensitivity to variations in the environmental refractive index [41–46]. In our investigation, we incorporated an artificial geometric structure surrounding a black phosphorus device and studied its enhanced transmission effects using the FDTD method, as depicted in Fig. 4. Our findings indicate that the geometric characteristics of the artificial geometric structure significantly influence light field distribution, conductivity and generation number. By carefully selecting the shape and periodicity of the artificial geometric structure, we can achieve optimal transmission intensity. Theoretical analysis reveals that the transmission enhancement arises from the interaction between localized surface plasmons and surface polarized plasmons.

In the ring artificial geometric structure, the light field exhibits axial symmetry, converging toward the center of the ring with a central intensity reaching 3 V/m, while distribution remains concentrated within the ring. Conversely, the fan-shaped artificial geometric structure displays light concentration at the center of the fan, characterized by a compact distribution with minimal axial extension. The semicircular artificial geometric structure presents a light field that is distributed along both the inner and outer edges, demonstrating a centrosymmetric distribution, with no significant intensity variance among different regions.

The ring structure induces specific interference and diffraction effects within the ring area, leading to a concentrated and uniform light field distribution. The central region benefits from intensified light intensity due to the superposition of multiple beams. The fan shape restricts the direction of light propagation, resulting in primary light concentration at the fan's center, while reflection and refraction along the fan's edge impede light from extending axially. The symmetry of the semicircular design provides similar propagation paths for light along the inner and outer edges, resulting in a more uniform light field distribution.

As depicted in Fig. 4d and e, while the shape of the artificial geometric structure does not significantly influence carrier separation efficiency, it does markedly affect conductivity. Devices with a ring artificial geometric structure exhibit significantly higher conductivity compared to those with semicircular or fan-shaped structures, displaying greater sensitivity to bias voltage. The conductivity shows more

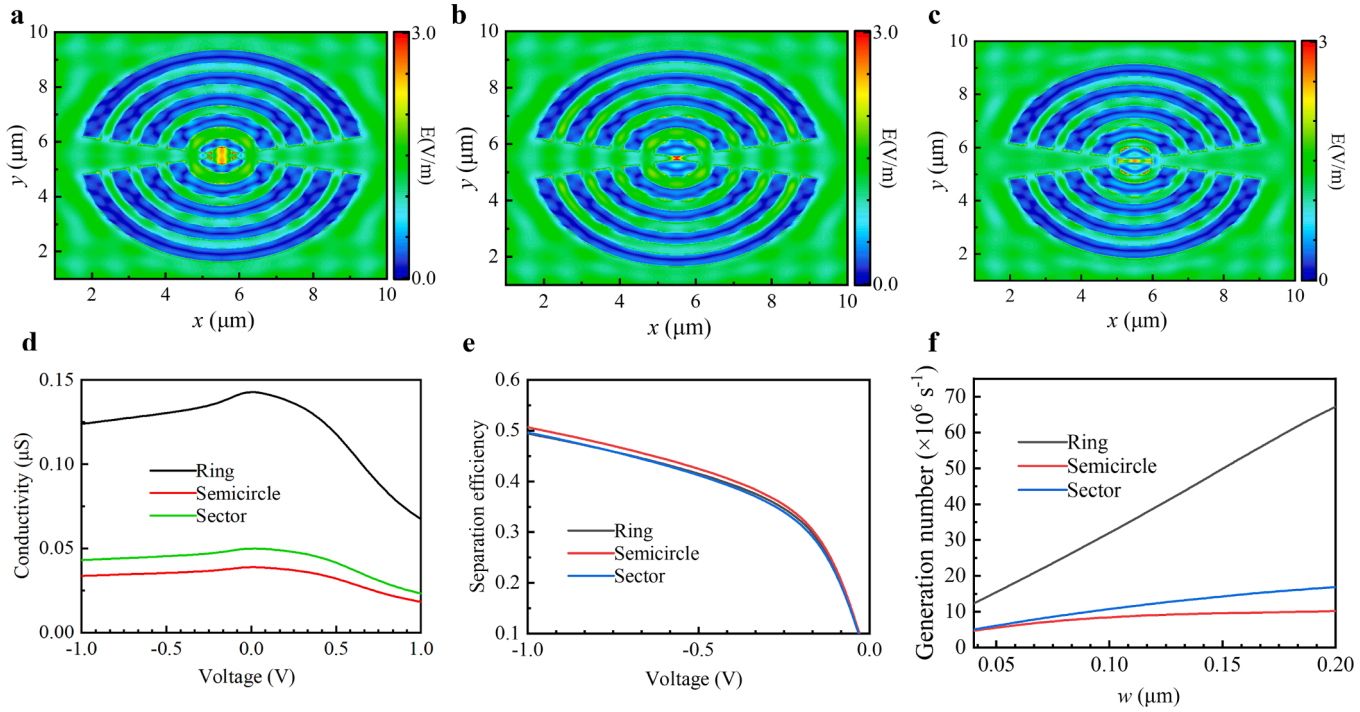


Fig. 4. Optical distribution simulation results for a device featuring artificial geometric structures. (a) The optical field distribution with a ring-shaped artificial geometric structure. (b) The optical field distribution with fan-shaped artificial geometric structure. (c) The optical field distribution with semicircular artificial geometric structure. (d) Simulated results demonstrating conductivity variations for different artificial geometric shapes under various bias conditions. (e) Simulated results illustrating separation efficiency across different artificial geometric shapes under varying reverse bias conditions. (f) Simulated results related to the generation number for distinct artificial geometric structures at different channel width.

variation under forward bias than under reverse bias, which is crucial for minimizing dark current in the device.

Simulation analyses of the generation number for various artificial geometric structures, as shown in Fig. 4f, reveal that, as the channel width increases, the generation number of charge carriers also escalates. In semi-circular and sector structures, this increase is relatively modest

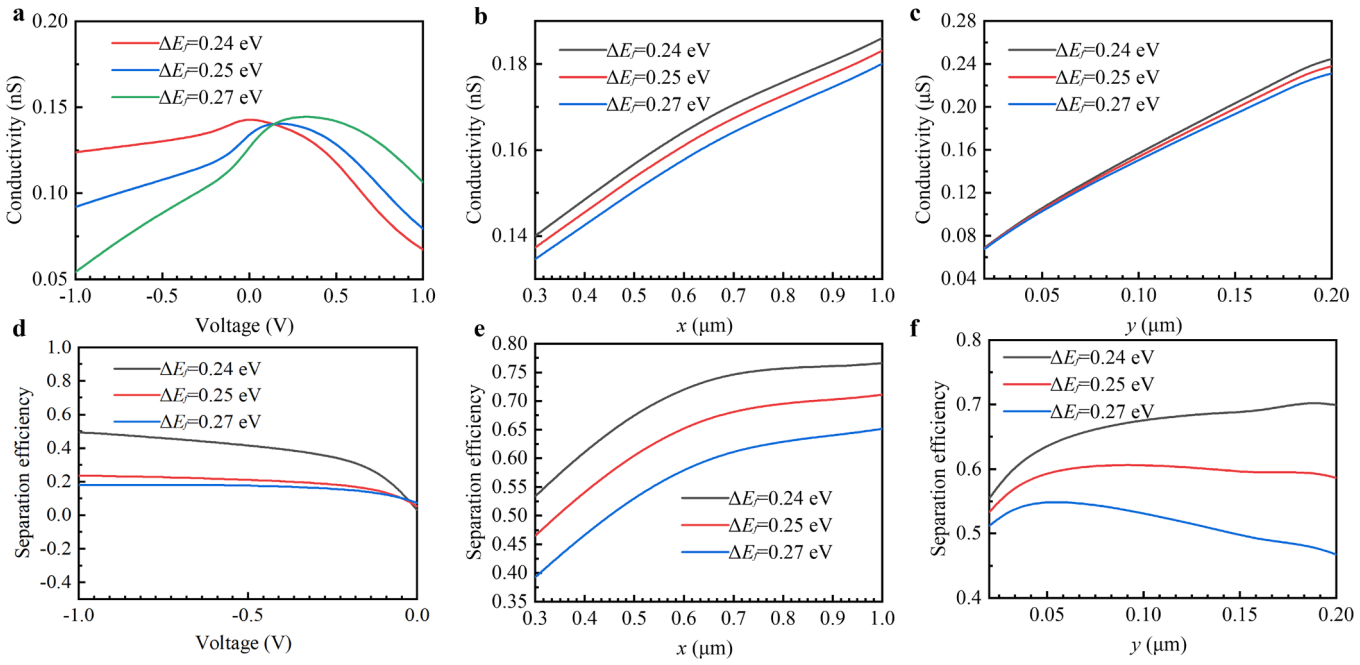


Fig. 5. Calculation result of photogenerated carrier separation efficiency and conductivity with different parameters in an artificial geometric structured light field. (a) The conductivity was assessed at different bias voltages while varying the Fermi energy level difference. (b) The conductivity was evaluated across different Fermi energy level differences at varying lengths of the system (c) The conductivity was measured with respect to different Fermi energy level differences at varying widths of the system. (d) The separation efficiency was determined under varying bias conditions and different Fermi energy level differences. (e) The separation efficiency was analyzed for different Fermi energy level differences across various lengths. (f) The separation efficiency was further examined with respect to different Fermi energy level differences at varying widths.

and tends to stabilize over time. This phenomenon could be attributed to the geometric configuration and the resultant electric field distribution, which limit the efficiency of carrier generation and recombination processes. Conversely, in ring artificial geometric structures, the relationship between the increase in generation number and channel width approximates a linear trend. This may be due to the symmetrical geometry promoting a more uniform electric field distribution, thereby facilitating a more efficient generation and recombination of charge carriers that correlates closely with the channel width.

Comparative analysis indicates that the ring artificial geometric structure, with its heightened light field intensity and broader distribution area, promotes effective interactions between light and materials. This localization effect ensures that energy is concentrated in specific regions, enhancing physical processes such as electronic transitions within materials and further amplifying light-material interactions. By optimizing the parameters of the ring artificial geometric structure, we aim to further enhance the interaction efficiency between light and materials, ultimately improving the performance of the device.

We simulated the effects of various parameters on conductivity and the separation efficiency of photogenerated carriers in a black phosphorus device integrated with an artificial geometric structure (Fig. 5). Under Fermi energy level differences of (ΔE_f = 0.24 eV, 0.25 eV and 0.27 eV), we observed that conductivity varies with the applied bias voltage, showing an increase or decrease depending on the bias conditions. Specifically, as reverse bias voltage increases, the Fermi energy level difference also rises, resulting in more pronounced changes in conductivity. Conversely, in the forward bias region, the behavior is inverted.

In the reverse bias regime, lower Fermi energy level differences correlate with higher separation efficiency of photogenerated carriers; stronger voltages further enhance this efficiency. The increase in reverse bias affects the band structure, altering the distribution of electrons and holes and causing shifts in the Fermi level. As the Fermi energy level difference rises, carrier transport experiences more hindrance, leading to greater fluctuations in conductivity. Under reverse bias, fewer carriers are available for conduction, decreasing carrier concentration and thus weakening conductivity.

With the augmentation of both the length and width of the junction (Fig. 5b and c), there is a corresponding increase in conductivity. However, this increase is observed to occur at a diminishing rate. This can be explained by the fact that, although an expanded junction area accommodates a greater number of charge carriers that contribute to conduction, the influence of scattering processes and other intrinsic material properties intensifies as the dimensions increase. As a result, the marginal gains in conductivity diminish due to the interplay between these competing phenomena.

Under reverse bias (Fig. 5d), the separation efficiency improves with a smaller Fermi level difference, reflecting that a smaller difference results in minimal band structure alteration, enabling easier electron-hole separation. Higher voltages not only amplify the electric field's impact but can also excite more carriers, thereby increasing the number of participating carriers and enhancing separation efficiency.

The simulation also examined the influence of channel length and width in thin-layer materials on conductivity and photogenerated carrier separation efficiency (Fig. 5e and f). We found that increased channel length results in higher conductivity and lower dark current, particularly with reduced Fermi energy level differences. A longer transport channel means a more extended path for carrier movement, resulting in a higher likelihood of encountering scattering and recombination events, ultimately boosting overall conductivity. However, increased scattering can also enhance carrier migration resistance, especially in the dark state, consequently decreasing dark current.

The separation efficiency of photogenerated carriers initially increases with channel length but tends to saturate at longer lengths. Lower Fermi energy levels correlate with higher separation efficiency. As channel length increases, the travel time and distance for carriers also expand, providing more opportunities for particles to separate under the electric field. However, excessively long channels increase the probability of carrier recombination, which can lead to saturation of separation efficiency. Moreover, beyond a certain width, there may be no further increase in separation efficiency, and it could potentially decline.

4. Conclusion

In summary, addressing the challenge of uneven material thickness arising from the mechanical exfoliation of two-dimensional materials that form natural heterojunctions, we have engineered narrow-channel heterojunction devices. Through a combination of theoretical calculations and simulations, we investigated the influence of channel length and width of the thin-layer material, as well as the applied voltage, on the characteristics of the built-in electric field, including its intensity and spatial distribution. Our findings reveal that the distribution range of the built-in electric field is predominantly determined by the applied bias and channel length, whereas the intensity of the electric field is chiefly influenced by both the bias and channel width. Additionally, we designed various artificial geometric structures to enhance the optical field. The results demonstrate that the ring-shaped artificial geometric structure provides the most extensive optical field distribution area and exhibits superior localization effects. By analyzing conductivity and the efficiency of photogenerated carrier separation, we conducted a comprehensive examination of the impact of different parameters at the microscopic mechanism level. Notably, the ring-shaped artificial geometric structure displays enhanced conductivity, which significantly mitigates dark current. Through the careful adjustment and selection of parameters, we can effectively enhance sensitivity, improve noise characteristics, and optimize response speed. Our engineered narrow-channel heterojunction devices not only solve existing challenges related to material uniformity but also reveal new avenues for high-performance applications in various fields, positioning them at the forefront of next-generation electronic and optoelectronic technologies in optoelectronics, sensing technologies and quantum devices in both microscopic mechanism insights and tailored responses to external conditions.

CRediT authorship contribution statement

Min Luo: Writing – review & editing, Writing – original draft, Validation, Methodology, Investigation, Formal analysis, Data curation, Conceptualization. **Haonan Ge:** Writing – review & editing, Methodology, Data curation, Conceptualization. **Shuning Liu:** Writing – review & editing, Writing – original draft. **Runzhang Xie:** Writing – review & editing, Project administration. **Fang Zhong:** Writing – review & editing, Conceptualization.

Declaration of competing interest

The authors declare that they have no known competing financial interests or personal relationships that could have appeared to influence the work reported in this paper.

Acknowledgements

This work was supported by National Natural Science Foundation of China (grant nos. 62205360, and 62305079), Natural Science Foundation of Shanghai (grant no. 22ZR1472500) and China Postdoctoral Science Foundation (2022M713260).

Data availability

Data will be made available on request.

References

[1] A. Geim, I. Grigorieva, Van der Waals heterostructures, Nature 499 (2013) 419–425, https://doi.org/10.1038/nature12385.
[2] K.S. Novoselov, et al., 2D materials and van der Waals heterostructures, Science 353 (2016) aac9439, https://doi.org/10.1126/science.aac9439.
[3] J. Schaibley, et al., Valleytronics in 2D materials, Nat. Rev. Mater. 1 (2016) 16055, https://doi.org/10.1038/natrevmats.2016.55.
[4] Z. Wang, et al., Giant infrared bulk photovoltaic effect in tellurene for broad-spectrum neuromodulation, Light Sci. Appl. 13 (2024) 277, https://doi.org/10.1038/s41377-024-01640-w.
[5] Y.F. Chen, et al., Unipolar barrier photodetectors based on van der Waals heterostructures, Nat. Electron. 4 (2021) 357–363, https://doi.org/10.1038/s41928-021-00586-w.
[6] W.D. Hu, X.S. Chen, Z.H. Ye, W. Lu, A hybrid surface passivation on HgCdTe long wave infrared detector with in-situ CdTe deposition and high-density Hydrogen plasma modification, Appl. Phys. Lett. 99 (2011) 091101, https://doi.org/10.1063/1.3633103.
[7] W.D. Hu, et al., 128 × 128 long-wavelength/mid-wavelength two-color HgCdTe infrared focal plane array detector with ultralow spectral cross talk, Opt. Lett. 39 (2014) 5184–5187, https://doi.org/10.1364/OL.39.005184.
[8] F.X. Dai, et al., anomalous non-equilibrium state response of long-wavelength HgCdTe infrared detectors, IEEE Electron. Device Lett. 45 (1) (2024) 16–19, https://doi.org/10.1109/LED.2023.3335419.
[9] D. Ke, et al., High transmission efficiency long-wave infrared multispectral modulation array based on nanogap engineering, Infrared Phys. Technol. 142 (2024) 105559, https://doi.org/10.1016/j.infrared.2024.105559.
[10] D.N. Basov, et al., Polaritons in van der Waals materials, Science 54 (2016) aag1992, https://doi.org/10.1126/science.aag1992.
[11] G. Haonan, et al., Artificial micro- and nano-structure enhanced long and very long-wavelength infrared detectors, Acta Phys. Sin. 71 (11) (2022) 110703, https://doi.org/10.7498/aps.71.20220380.
[12] K. Deng, et al., High transmission efficiency long-wave infrared multispectral modulation array based on nanogap engineering, Infrared Phys. Technol. 142 (2024) 105559, https://doi.org/10.1016/j.infrared.2024.105559.
[13] C. Sun, et al., Tunable narrow-band single-channel add-drop integrated optical filter with ultrawide FSR, PhotoniX 3 (2022) 12, https://doi.org/10.1186/s43074-022-00056-2.
[14] M. Kim, et al., Intrinsic Correlation between electronic structure and degradation: from few-layer to bulk black phosphorus, Angew. Chem. Int. Ed. 58 (2019) 3754, https://doi.org/10.1002/anie.201811743.
[15] Z. Wang, et al., Controllable doping in 2D layered materials, Adv. Mater. 33 (2021) 2104942, https://doi.org/10.1002/adma.202104942.
[16] C. Wang, et al., On-chip optical sources of 3D photonic integration based on active fluorescent polymer waveguide microdisks for light display applications, PhotoniX 4 (2023) 13, https://doi.org/10.1186/s43074-023-00090-8.
[17] J.-H. Duan, J.-N. Chen, Recent progress of near-field studies of two-dimensional polaritonics, Acta Phys. Sin. 68 (11) (2019) 110701, https://doi.org/10.7498/aps.68.20190341.
[18] T. Low, et al., Polaritons in layered two-dimensional materials, Nature Mater 16 (2017) 182–194, https://doi.org/10.1038/nmat4792.
[19] J. Wang, et al., Deep multiband photodetectors enabled by reconfigurable band alignment in van der Waals heterostructures, Optica (2024), https://doi.org/10.1364/OPTICA.519888.
[20] L. Li, et al., Black phosphorus field-effect transistors, Nat. Nanotech. 9 (2014) 372–377, https://doi.org/10.1038/nnano.2014.35.
[21] A.S. Rodin, A. Carvalho, A.H. Castro Neto, Strain-induced gap modification in black phosphorus, PhysRevLett. 112 (2014) 176801, https://doi.org/10.1103/PhysRevLett.112.176801.
[22] H. Asahina, A. Morita, Band structure and optical properties of black phosphorus, J. Phys. c: Solid State Phys. 17 (1984) 1839, https://doi.org/10.1088/0022-3719/17/11/006.
[23] H. Yuan, et al., Polarization-sensitive broadband photodetector using a black phosphorus vertical p–n junction, Nat. Nanotech. 10 (2015) 707–713, https://doi.org/10.1038/nnano.2015.112.
[24] Q. Guo, et al., Black phosphorus mid-infrared photodetectors with high gain, Nano Lett. 16 (7) (2016) 4648–4655, https://doi.org/10.1021/acs.nanolett.6b01977.
[25] J. Bullock, et al., Polarization-resolved black phosphorus/molybdenum disulfide mid-wave infrared photodiodes with high detectivity at room temperature, Nat. Photon 12 (2018) 601–607, https://doi.org/10.1038/s41566-018-0239-8.
[26] Y.S. Zhang, et al., Wavelength-tunable mid-infrared lasing from black phosphorus nanosheets, Adv. Mater. 32 (2020) 1808319, https://doi.org/10.1002/adma.201808319.
[27] J. Wang, et al., Mid-infrared polarized emission from black phosphorus light-emitting diodes, Nano Lett. 20 (5) (2020) 3651–3655, https://doi.org/10.1021/acs.nanolett.0c00581.
[28] H. Wang, et al., Recent advances in two-dimensional photovoltaic devices, J. Semicond. 45 (5) (2024) 051701, https://doi.org/10.1088/1674-4926/45/5/051701.
[29] A. Nemilentsau, T. Low, G. Hanson, Anisotropic 2D materials for tunable hyperbolic plasmonics, PhysRevLett. 116 (2016) 066804, https://doi.org/10.1103/PhysRevLett.116.066804.
[30] Y. Yao, et al., High-responsivity mid-infrared graphene detectors with antenna-enhanced photocarrier generation and collection, Nano Lett. 14 (2014) 3749–3754, https://doi.org/10.1021/nl50185.
[31] J. Fujikata, et al., Si Nano-Photodiode with a Surface-Plasmon Antenna for SiON Waveguide-Integrated Structure, in: LEOS 2007 - IEEE Lasers and Electro-Optics Society Annual Meeting Conference Proceedings, IEEE, 2007, pp. 929–930, https://doi.org/10.1109/LEOS.2007.4382715.
[32] R.D.R. Bhat, et al., Enhancing the signal-to-noise ratio of an infrared photodetector with a circular metal grating, Opt. Express 16 (2008) 4588–4596, https://doi.org/10.1364/OE.16.004588.
[33] V. Giannini, et al., Plasmonic nanoantennas: fundamentals and their use in controlling the radiative properties of nanoemitters, Chem. Rev. 111 (2011) 3888–3912, https://doi.org/10.1021/cr1002672.
[34] Taflove, A. & Hagness, S. C. Computational Electrodynamics: The Finite-Difference Time-Domain Method (Artech House, 2005).
[35] T. Tene, et al., THz plasmonics and electronics in germanene nanostrips, J. Semicond. 44 (2023) 102001, https://doi.org/10.1088/1674-4926/44/10/102001.
[36] H. Choi, et al., Broadband electromagnetic response and ultrafast dynamics of few-layer epitaxial graphene, Appl. Phys. Lett. 94 (17) (2009) 172102, https://doi.org/10.1063/1.3122348.
[37] G.W. Hanson, Dyadic Green's functions and guided surface waves for a surface conductivity model of graphene, J. Appl. Phys. 103 (6) (2008) 064302, https://doi.org/10.1063/1.2891452.
[38] A.S. Dashkov, et al., An advanced theoretical approach to study super-multiperiod superlattices: theory vs experiments, J. Semicond. 45 (2) (2024) 022701, https://doi.org/10.1088/1674-4926/45/2/022701.
[39] Q. Li, et al., Direct mapping and characterization of the surface local field in InGaAs/InP avalanche photodetectors, Infrared Phys. Technol. 123 (2022) 104162, https://doi.org/10.1016/j.infrared.2022.104162.
[40] D.E. Aspnes, et al., Optical properties of AlxGa1-xAs, J. Appl. Phys. 60 (1986) 754–767.
[41] P. Kumar, et al., Thickness and electric-field-dependent polarizability and dielectric constant in phosphorene, PhysRevB 93 (2016) 195428, https://doi.org/10.1103/PhysRevB.93.195428.
[42] N.S. Azar, et al., Bull's eye grating integrated with optical nanoantennas for plasmonic enhancement of graphene long-wave infrared photodetectors, Appl. Phys. Lett. 114 (9) (2019) 091108, https://doi.org/10.1063/1.5082664.
[43] B. Deng, et al., Efficient electrical control of thin-film black phosphorus bandgap, Nat. Commun. 8 (2017) 14474, https://doi.org/10.1038/ncomms14474.
[44] R.J. Suess, et al., Mid-infrared time-resolved photoconduction in black phosphorus, 2D Mater. 3 (2016) 041006, https://doi.org/10.1088/2053-1583/3/4/041006.
[45] Z. Yang, et al., Control of EOT of subwavelength metal bullseye structures by coaxial nano-columns, Opto-Electro. Eng. 45 (11) (2018) 180207, https://doi.org/10.12086/oee.2018.180207.
[46] S.K. Zhu, et al., Harnessing disordered photonics via multi-task learning towards intelligent four-dimensional light field sensors, PhotoniX 4 (2023) 26, https://doi.org/10.1186/s43074-023-00102-7.